PerfECT Design Tool: Electric Vehicle Modelling and Experimental Validation

Original
PerfECT Design Tool: Electric Vehicle Modelling and Experimental Validation / de Carvalho Pinheiro, Henrique. - In: WORLD ELECTRIC VEHICLE JOURNAL. - ISSN 2032-6653. - ELETTRONICO. - 14:12(2023), pp. 1-28. [10.3390/wevj14120337]

Publisher:
MDPI

Published
DOI:10.3390/wevj14120337

World Electric Vehicle Journal

Article

PerfECT Design Tool: Electric Vehicle Modelling and Experimental Validation

Henrique de Carvalho Pinheiro

Department of Mechanical and Aerospace Engineering (DIMEAS), Politecnico di Torino, 10138 Turin, Italy; henrique.decarvalho@polito.it

Abstract: This article addresses a common issue in the design of battery electric vehicles (BEVs) by introducing a comprehensive methodology for the modeling and simulation of BEVs, referred to as the "PerfECT Design Tool". The primary objective of this study is to provide engineers and researchers with a robust and streamlined approach for the early stages of electric vehicle (EV) design, offering valuable insights into the performance, energy consumption, current flow, and thermal behavior of these advanced automotive systems. Recognizing the complex nature of contemporary EVs, the study highlights the need for efficient design tools that facilitate decision-making during the conceptual phases of development. The PerfECT Design Tool is presented as a multi-level framework, divided into four logically sequential modules: Performance, Energy, Currents, and Temperature. These modules are underpinned by sound theoretical foundations and are implemented using a combination of MATLAB/Simulink and the vehicle dynamics software VI-CRT. The research culminates in the validation of the model through a series of experimental maneuvers conducted with a Tesla Model 3, establishing its accuracy in representing the mechanical, electrical, and thermal behavior of BEVs. The study's main findings underscore the viability of the design tool as an asset in the initial phases of BEV design. Beyond its primary application, the tool holds promise for broader utilization, including the development of active control systems, advanced driver assistance systems (ADAS), and solutions for autonomous driving within the domain of electric vehicles.

Keywords: electric vehicles; modelling and simulation; design methodology; vehicle dynamics; electric powertrain; batteries

Citation: de Carvalho Pinheiro, H. PerfECT Design Tool: Electric Vehicle Modelling and Experimental Validation. *World Electr. Veh. J.* **2023**, *14*, 337. https://doi.org/10.3390/wevj14120337

Academic Editor: Joeri Van Mierlo

Received: 2 November 2023
Revised: 27 November 2023
Accepted: 30 November 2023
Published: 5 December 2023

1. Introduction

The electric vehicle is not a 21st century invention. At the beginning of the automotive industry in the early 1900s, three main architectures dominated the automobile market: 40% were steam powered, 38% were electric and just 22% used gasoline [1]. Electric vehicles were seen as a very convenient solution since they were quiet, did not suffer from vibrations or fumes, and the engines, unlike those that needed to be cranked, required little effort to start.

These advantages were counterposed by some limitations related to their range (no higher than 50–65 km), maximum speed (limited to around 30 km/h), and the length of time to recharge. It is easy to find similarities to the current challenges of EVs.

For that reason, after a short period of market success, especially in urban settings, electric vehicles were practically completely substituted by the ICE of Benz and, soon after, the ubiquitous Model T from Ford. For decades, the EV market was almost null, apart from special applications and some very punctual examples [2].

Interest in the technology gained momentum in the 1990s, with many examples of mass market proposals and big players, such as General Motors, announcing their intentions to produce new electric models [3]. An important driver for this revival was regulatory, with the first version of the Zero-Emission Vehicles (ZEV) mandate being announced in California [4].

Indeed, the importance of the EV movement from the beginning of the 21st century is twofold: technological and regulatory. If, from one side, key technologies like lithium batteries started to be applied to vehicles and greatly improved EV performance [5,6], from the other side, the restrictions imposed by policy are a constant pressure for the quick development of such technologies.

The European emission standards directives are among the most important initiatives for pollution control in the mobility sector. Since 1992, when the Euro 1 standard was put in place [7], a continuous effort to restrict the amount of emissions from vehicles has become part of the European scenario, leading to many other similar regulations around the world.

The trend created by the European Commission continues until today, with ever higher levels of constraint on emissions. Euro 7 is expected by 2025 [8] and programs like the "Fit for 55" [9] promise severe limitations on ICE vehicles in the European market, including a possible 100% CO_2 emissions reduction by 2035 [10], making it virtually impossible for big carmakers to ignore the electrification tendency.

The future of the EV market looks bright, with the favorable legislation push creating demand for zero-emission vehicles at the same time that technologies like batteries continue to increase their performance and see their prices drop [11]. Most business reports and market analyses put the estimates of market growth in the vicinity of 20% CAGR [12,13], mostly concentrated in the Chinese, European and US markets.

This outlook does not come, of course, without a series of challenges. The recycling of batteries [14–16], safety [17,18], recharging times and limitations of the grid [19–21], scarcity of key-materials [22] and energy consumption for manufacturing [23] are important threats.

The work presented in [24] analyzes whether or not this automotive solution will be able to maintain its title as the main personal form of mobility, or meet the challenge of achieving the "six zero goals" of Zero Emissions, Zero Energy, Zero Congestion, Zero Accident, Zero Empty, and Zero Cost. The authors forecast that new evolutions in technology can help the sector to sufficiently evolve.

It is important to evaluate the overall impact of new forms of mobility, not just in terms of local pollutants or overall emissions, but with a broader approach. This kind of analysis can be performed with LCA (Life Cycle Assessment) tools, as shown in [25]. This work proposes a sound methodology for vehicle impact evaluation and concludes that, even with a power mix dominated by fossil fuel strategies, EVs can be effective in reducing gas emissions in the overall LCA.

New technologies are emerging in terms of energy storage, and electrochemical sources continue to promise evolution and performance improvements [26–30] beyond the current levels of the market [6]. New technologies and chemistries such as lithium air [31], lithium-sulphur [32,33], sodium superoxide [34,35] and solid-state [36–38] are promising solutions, but are not yet ready to be deployed in the market. Other sources of energy [39–41] and the continuous effort to reduce mass [42–49] and increase energy efficiency [50–52] also work towards a more electrified future.

In the current scenario for the automotive field, the competition is always fiercer, both because of the creation of huge sector empires (through the mergers and acquisitions of big players) and due to the pressure of new entrants from emerging markets. These pressures create, more than ever, the necessity to reduce the time-to-market of new models and to trim all possible wastes (of time and money) during the development phases.

Engineering digital tools are not new in the sector, and they play a crucial role in today's vehicle development. It is unthinkable to produce even a first prototype of a component without several loops of Computational Aided Design (CAD), Computational Aided Engineering (CAE), and Computational Fluid Dynamics (CFD) and the use of many other specialized tools. It is natural that during the evolution of the product development workflow, these tools are used to support the process change.

It is no secret that vehicle development is a complex task; among the many different subsystems and their often interdependent and complex relations, it must be considered also the not-so-clear subjective evaluations and needs of the different users. A car must have high power, but low fuel consumption; it must be spacious, but aerodynamically streamlined; it must be beautifully shaped, but its bodywork must be easily manufacturable; it must have the most advanced technologies but the price must be affordable. Designing a vehicle is as much an art as it is engineering.

These compromises are as true for EVs as they are for ICE vehicles. One main difference, though, is the timing of these two vehicle technologies: ICE vehicles were born and gained popularity at the beginning of the XX century, a period with a much less globalized and complex economy and much less technology at the disposal of designers and engineers. The methods used for the development of the first ICEVs cannot be the same as those used to create this new batch of automobiles.

A classic approach to product development is the so-called V-model [53], in which the workflow begins with broad-view requirements analysis and performance definition at then vehicle level, then moves to the design and definition of the architectures and solutions at the sub-system level and finally to the implementation phase, in which the specific characteristics of the components are defined.

This first “leg” of the V-shape incrementally increases the level of detail and the specialization level requested. At the end of the product definition and execution, the validation stages begin, where the final product will be compared to the initially defined performance targets. This phase happens in a reverse order, from the requirement verification of the single components to the sub-systems, to the full-vehicle validation. Clearly this process is not linear, meaning that every time a performance is not met during the validation phase, or a problem is noticed in the component design phase, it can be necessary to loop back to the previous stages to adjust and adapt them accordingly.

This V-shape approach with design loops can generate problems and delays in the launch workflow, especially when big gaps in performance are outlined in the very final phases of testing. More modern strategies tend to include verification phases earlier on in the process to reduce the impact of the changes and expedite the development using approaches such as the Multiple V-model and incremental V-model [53]. However, the general philosophy of narrowing down and specializing during the design, then building up and increasing integration in the validation phase is still in place.

Following this framework, what is necessary, in terms of simulation and design tools, to support EV development?

It is clear from the workflow that the level of specialization and detail increases with time. It is also true that the single components of an E-PWT already possess (apart, maybe, from batteries) a plethora of instruments to support their development. Arguably, the most pressing challenges occur at the beginning of the design process.

One might think that the concept phases of the engineering process are an easier task than the implementation, however this stage is full of uncertainties and plays a critical role in the success of a new endeavor. At the very start, it is usual not to have a clear picture of vehicle layout, feasibility, and overall performance attainable. Making choices in this kind of environment is undoubtedly hard, thus having a support tool becomes handy. Such a tool must be sufficiently precise and at the same time cannot depend on a full set of vehicle parameters, still being studied, and decided.

This article presents multi-level process for modelling and design of electric vehicles, entitles “PerfECT Design Tool”. More specifically, the design tool is divided into four independent but logically sequential modules (Performance, Energy, Current and Temperature–motivating the acronym), whose theoretical base and implementation details are presented in the following sessions. After laying out the structure of the tool, a practical application and experimental validation campaign are presented, featuring the case study of a Tesla Model 3.

The main contribution of the article is the logic and method proposed for the streamlined design process of new electric vehicles, specifically regarding the first phases of the product development process, always keeping in mind that for each component or subsystem there are dedicated tools and methods that run in parallel. Apart from this, other uses are also envisioned; for example, the method can be used as a platform for the design of active control systems [54–58], ADAS and autonomous driving [59,60] solutions for EVs. The novelty of the solution is its multi-step nature, modularity, and flexibility of implementation which, in comparison with commercial tools, can offer a more tailored experience to professionals working on different phases of the design process.

The article will show the modelling theoretical background used for the development in Section 2, the actual implementation of the model in its various stages in Section 3 and the experimental validation of the algorithm in Section 4.

2. Modelling Theoretical Background

This session briefly presents some of the essential models used that are related to: the lateral dynamics of vehicles, handling, and stability; longitudinal dynamics, drivability and energy efficiency; the main components of electric powertrains, namely batteries and electric motors; and finally, the thermal phenomena taking place in EVs such as heat generation, and heat transfer.

2.1. Lateral Dynamics Modelling

Vehicle dynamics is a branch of automotive engineering that aims to describe the responses of automobiles when performing maneuvers. The history of vehicle dynamics as a consolidated branch of scientific inquiry begins with motorsports. The need to push the limits of racecars and improve their performance during challenging track competitions obliged engineers to formally study the physical phenomena behind vehicle dynamics, in addition to the "trial and error" method that was once the main approach. As a matter of fact, the clear objectives and rigid restrictions of racing provide an excellent framework for understanding vehicle behavior, as extensively shown by Milliken in their textbook [61].

When it comes to lateral behavior, arguably the most relevant study regards the controllability of the vehicle by means of steering inputs. The steering wheel is the main interface between driver and automobile; thus, it becomes essential to establish the response dynamics for each driving condition.

Commonly, when describing the most elementary models of lateral dynamics, the vehicle is represented by a reduced version of the four-wheel layout, in which left and right-hand sides are collapsed in the so-called "bicycle model" (Figure 1). This single-track approach allows for a leaner description and less cumbersome equations, without significantly jeopardizing accuracy.

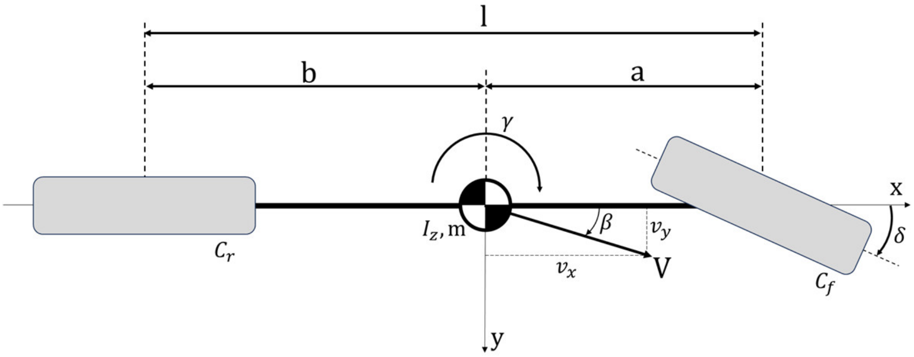

Figure 1. The bicycle model vehicle diagram [62].

By defining the front and rear forces developed in the tires as linear relations with α through the tire stiffness coefficients C_F and C_R, it is relatively easy to establish the relation between δ and the other parameters defining the lateral motion (lateral acceleration a_y, curvature radius R, yaw rate γ and vehicle sideslip β), which are relevant when reproducing their final form. The explicit equations can be written in an elegant, reduced form:

$$M_z = I_z\dot{r} = N_\beta\beta + N_r r + N_\delta\delta \tag{1}$$

$$F_y = mV(r + \dot{\beta}) = Y_\beta\beta + Y_r r + Y_\delta\delta \tag{2}$$

taking advantage of the concept of "Derivative Notation". As the name suggests, the terms N_β, N_r, N_δ, Y_β, Y_r, and Y_δ bundle the relevant physical parameters of the vehicle, directly defining the partial derivative of $\dot{r}$ and $\dot{\beta}$ with respect to each vehicle state (sidelip angle and yaw rate) or control state (steering angle). The values of the derivatives are defined as:

$$\begin{cases} Y_\beta = \frac{dF_y}{d\beta} = (C_F + C_R)\,, & N_\beta = \frac{dM_z}{d\beta} = (aC_F - b\,C_R) \\ Y_r = \frac{dF_y}{dr} = \frac{1}{V}(aC_F - bC_R)\,, & N_r = \frac{dM_z}{dr} = \frac{1}{V}(a^2C_F + b^2C_R) \\ Y_\delta = \frac{dF_y}{d\delta} = -C_F\,, & N_\delta = \frac{dM_z}{d\delta} = -aC_F \end{cases} \tag{3}$$

The most convenient and compact way to represent the dynamic equations is the state space matrixial approach. Considering the decoupling between lateral and longitudinal dynamics, it is possible to write the same set of equations as

$$\dot{x} = Ax + Bu \tag{4}$$

where

$$x = \begin{pmatrix} \beta \\ \gamma \end{pmatrix},\ A = \begin{pmatrix} \frac{C_f + C_r}{mv_x} & \frac{aC_f - bC_r}{m{v_x}^2} - 1 \\ \frac{aC_f - bC_r}{I_z} & \frac{a^2C_f + b^2C_r}{I_z{v_x}^2} \end{pmatrix},\ u = \begin{pmatrix} \delta \\ M_z \end{pmatrix},\ B = \begin{pmatrix} -\frac{C_f}{mv_x} & 0 \\ -\frac{aC_f}{I_z} & \frac{1}{I_z} \end{pmatrix} \tag{5}$$

The "bicycle model" is a simple, interesting, and very insightful means to study the macro-behavior of a vehicle; however, its precision and robustness are limited. One common method to increase model complexity resides in the use of a multibody dynamics approach. However, at the very beginning of the design process of a vehicle, it is difficult to obtain all the information necessary to develop a full-vehicle multibody model.

To reduce both the complexity of the data inputs, and computational effort, a simpler version of the multibody system can be used. Instead of describing each mechanical component separately, and writing all six equations of motion, a reduced mechanical system can be created, in which only five elements are included: the vehicle body and the four wheels. This model, called the "Isolated Vehicle" in the textbook by Genta and Morello [63], considers one of the mechanical elements (usually the vehicle body) as the main body with a full six degrees-of-freedom (DOF) motion description, while the secondary bodies present only the "free" DOF after considering their relationship with the main body in terms of joints. More specifically, in a passenger vehicle, the body has 6 DOF and each one of the wheels has, at least, one DOF with respect to the body (the wheel travel).

Following the approach suggested by [63], the steps required to derive the equations of motion of the system are the computation of potential and kinetic energies, the virtual work of external forces, and the dissipation function followed by the definition of the equations of motion using Lagrange equations.

Regarding the suspension system, whilst it is not described by analytical kinematic relations (as in the multibody models) it is necessary to describe its motion—more specifically, the relative displacements of the wheels and body. The motion can be described as a function of the generalized coordinate ζ that represents the wheel travel distance. The motion in each direction of the general coordinate system can be written as a function of ζ and, therefore, interfaced with the rest of the equations. Each suspension arrangement will, thus, have a particular expression to represent its kinematics. In software solutions such as VI-CRT 2022 [64], it is possible to derive the curves representing the kinematic relations beforehand (by importing kinematic models from multibody software, by using their proprietary toolbox or manually inserting the desired diagrams) so that the tables are consulted to solve the numerical systems.

2.2. Longitudinal Dynamics Modelling

The main sources of resistance to the vehicle's motion are aerodynamic drag, tire rolling resistance, grade force, and transmission losses. Apart from the resistances themselves, it is also convenient to model the inertial effects to describe the longitudinal accelerations.

The **aerodynamic drag** represents the force generated by the resistance associated with the movement of the vehicle through the air. The most common way to represent such force is in

$$R_{aero} = \frac{1}{2}\rho V_r^2 S C_x \tag{6}$$

where ρ is the air density, V_r^2 is the longitudinal velocity of the vehicle relative to the air (considering the x component of the wind), S is the vehicle's front area and C_x is the drag coefficient.

The **rolling resistance** is a phenomenon that occurs when the tires are in motion. The elastomeric material in contact with the road will deform at the entrance of the contact patch and relax after sliding out of the contact zone, but all the energy used to compress the material will not be recovered, thus creating dissipation [65].

The energy necessary to overcome the tire deformation can be interpreted as a force, whose moment counterposes the forward movement of the wheel, either slowing it down or requesting an active torque from the powertrain to keep a constant speed. The rolling resistance is not easy to describe analytically, and it is usual to represent it as this experimental curve

$$R_{roll} = F_z\left(f_0 + kV^2\right) \tag{7}$$

where f_0, k, are experimental coefficients, F_z is the vertical load acting on the wheel, and V is the longitudinal speed. It is important to highlight that the vertical force acting on the vehicle will vary depending on the slope and aerodynamic effects. This approach is very convenient, since it incorporates all resistance effects related to the rolling motion, such as the bearing friction and the aerodynamic resistance generated by the rolling wheels, even if minor, with respect to the deformation effect.

The **grade force** is the component of the resistance to motion of a vehicle that depends directly on the slope of the road. More specifically, it is the projection of the vehicle's weight in the direction parallel to the road:

$$R_{grad} = m \cdot g \cdot sin(\alpha) \tag{8}$$

where α is the road slope.

Transmission losses are not properly a resistance force, in the sense that they form an internal resistance that is usually modeled as an efficiency η_t associated with the motor outputs:

$$P_{real} = \eta_t \cdot P_{motor} \tag{9}$$

The efficiency includes the contribution of gearbox, differential, shafts, bearings, hook joints, clutches and all other components connecting the motors to the wheel hubs. For electric vehicles, when single-gear setups are chosen, the number of components on the drivetrain are drastically reduced, as is their complexity and contribution to the overall efficiency. This efficient value can be assumed as fixed for a first analysis of the transmission system.

To properly calculate the accelerations of the vehicle, it is also necessary to consider the inertial contribution of spinning masses. Using an energetic approach, an expression of the “equivalent mass” m_e can be written from the relationship between the rotational speeds and the vehicle speed:

$$m_e = m + \frac{J_{wheel}}{R_e^2} + \frac{J_{trans}}{R_e^2\tau_f^2} + \frac{J_{motor}}{R_e^2\tau_f^2\tau_g^2} \tag{10}$$

where J_{wheel}, J_{trans} and J_{motor} are the moments of inertia of wheels, transmission, and motor respectively; R_e is the effective wheel radius; and τ_f and τ_g are the final and gearbox transmission ratios.

Knowing the external forces acting upon the vehicle, it is possible to describe its motion in the longitudinal direction:

$$\begin{cases} m\dot{V} = F_{x1} + F_{x2} + F_{x_{aer}} - m\cdot g\cdot sin(\alpha) \\ 0 = F_{z1} + F_{z2} + F_{z_{aer}} - m\cdot g\cdot cos(\alpha) \\ -m\cdot h_{CG}\cdot\dot{V} = F_{z1}a - F_{z2}b + m\cdot g\cdot h_{CG}\cdot sin(\alpha) - M_{aer} + F_{x_{aer}}h_{CG} \end{cases} \tag{11}$$

$$\begin{cases} F_{z_1} = \frac{mg}{l}\cdot\left[bcos(\alpha) - h_{CG}\sin(\alpha) - \frac{\rho S}{2mg}\left(C_x h_{CG} - C_{M_y} l + bC_z\right)V^2 - \frac{h_{CG}}{g}\dot{V}\right] \\ F_{z_2} = \frac{mg}{l}\cdot\left[acos(\alpha) + h_{CG}\sin(\alpha) - \frac{\rho S}{2mg}\left(-C_x h_{CG} + C_{M_y} l + aC_z\right)V^2 + \frac{h_{CG}}{g}\dot{V}\right] \end{cases} \tag{12}$$

2.3. Batteries

Side-by-side with the electric drive, the batteries are the core element of the E-PWT. Energy storage is a key part of the performance of EVs, determining their maximum capabilities in terms of power output and, at the same time, the range and total capacity of the EV [66].

Typical automotive batteries are composed of assemblies of battery cells, representing the basic electrochemical unit of the system. The cells are then grouped and connected in modules, which are connected to create the overall battery pack. To achieve targets of voltage and capacity, the cells and the modules are connected in series or in parallel.

The most widespread choice is the latter, namely using the Thévenin equivalent circuit approach. Typically, models use single or double polarization (meaning one or two RC blocks after the resistance R_0) as in Figure 2.

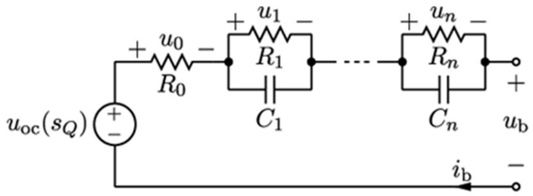

Figure 2. Dual polarization Thévenin circuit for electrochemical cell [67].

It is possible to directly derive the overall module/pack equivalent Thévenin circuit (composed of N_s identical cells in series and N_p identical cells in parallel) by computing their parameters R_0, R_1, R_2, C_1 and C_2 with straightforward arithmetic:

$$R_{i,eq} = \frac{N_s}{N_p}\cdot R_{i,cell}, \qquad C_{i,eq} = \frac{N_p}{N_s}\cdot R_{i,cell} \tag{13}$$

From the analysis of the response of the Thévenin circuit under different currents, it is possible to describe an important phenomenon related to the discharge rates. The faster the charge/discharge, the lower the efficiency of the cell and, thus, the lower the apparent capacity.

2.4. Electric Powertrain

In order to represent the motor's working principles and obtain the equations relating to the electric values, magnetic values, and the mechanical output, it is possible to approach the problem in a generalized approach as proposed in [68]. This kind of approach explores the electromagnetic relations using generalized reference systems with transformation matrixes to adapt the various possible forms of construction and arrangement of the EM.

Performing the transformation to the *d*–*q* axis with Clarke–Park transforms, one can find the general for equation for the voltages in matrix form as:

$$\begin{Bmatrix} V_d \\ V_q \end{Bmatrix} = R_s \begin{Bmatrix} I_d \\ I_q \end{Bmatrix} + \frac{d}{dt} \begin{Bmatrix} \lambda_d \\ \lambda_q \end{Bmatrix} + \omega \begin{bmatrix} 0 & -1 \\ 1 & 0 \end{bmatrix} \begin{Bmatrix} \lambda_d \\ \lambda_q \end{Bmatrix} \tag{14}$$

While the expression for the fluxes becomes

$$\begin{Bmatrix} \lambda_d \\ \lambda_q \end{Bmatrix} = \begin{bmatrix} L_d & L_{dq} \\ L_{qd} & L_q \end{bmatrix} \begin{Bmatrix} i_d \\ i_q \end{Bmatrix} + \begin{Bmatrix} \lambda_{md} \\ \lambda_{mq} \end{Bmatrix} \tag{15}$$

The terms of magnetization λ_{md} and λ_{mq} and the inductances L_d, L_q, L_{dq} and L_{qd}, depend on the specific type of PM machine studied and on the overall modeling hypothesis. For example:

- In the case of SPM machines, the disposition of the magnets in the rotor is isotropic, thus the terms $L_d = L_q$, while the flux generated by the PMs is aligned with the d-axis so $\lambda_{md} = \lambda_m$ while $\lambda_{mq} = 0$;
- For IPM the situation is equivalent regarding the PM flux, but the disposition of the PM is anisotropic, and made so that $L_d > L_q$;
- In the case of RM, the form of the rotor is such that the contribution of the inductances is much more influential in the d-axis, thus $L_d \gg L_q$, while no PM is included, so that $\lambda_{md} = \lambda_{mq} = 0$;
- For PM–SyR machines it remains true that $L_d \gg L_q$; however, the presence of PMs in the structure means that the contribution is $\lambda_{mq} = -\lambda_m$ while $\lambda_{md} = 0$.

Typical EM power and torque phases are represented as Figure 3. The first phase is represented by a constant maximum torque output (limited by the maximum current allowed) followed by a constant power phase (where the limit voltage also plays an important role) making the torque see a hyperbolic reduction with speed increments. Maximum rotational speed (due to maximum frequency) determines the limit EM speed–which could also be caused by mechanical limits, although not common.

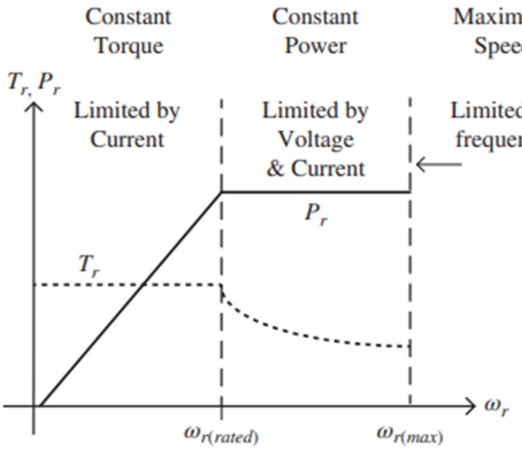

Figure 3. Typical torque and power curves for EMs [67].

The models aim to describe the EMs without an explicit implementation of the low-level control of the electric machines, which would entail an unfeasibly large computational burden [69]. To accomplish this goal, the electro-mechanical features of the EMs are defined through the application of the MTPA principle. By solving the optimization problem and finding the combination of i_d and i_q that simultaneously outputs the desired torque and minimizes the total absorbed current, it is possible to reasonably estimate the outcomes of a properly designed low-level control without explicit modelling. Specifically, in the case of the presented model, the MTPA-based results are encapsulated into look-up tables calculated a priori, since the chosen approach depends on the fixed resistance, reluctance, and magnetization parameters (instead of varying maps) [70]. This proves to accelerate considerably the simulation process.

2.5. Thermal Modelling

In EVs there are tighter limits of temperature so that the core components of the E-PWT can work properly.

Electric motors usually can endure temperatures as high as 140 °C in their coils, after which problems with electronic components or demagnetization of the PMs can occur and permanently damage the electric machine.

Power electronics also require close attention to heat generation and temperature management. Dealing with high currents and important switching frequencies, the problem of overheating is critical. The range of temperatures for which semi-conductors or other internal components in the inverters can deteriorate is similar to those of EMs, in the order of 150–175 °C.

Batteries, on the other hand, work with even more challenging constraints. The most suitable range of temperatures for Li-ion cells is between 15 °C and 35 °C. There are three main components contributing to the heat generation: motors, inverters, and batteries.

In Ems, there are four principal sources of heat: copper losses, iron losses, aerodynamic drag, and mechanical friction. For the purposes of modeling, it will be assumed that all energy associated with internal losses are converted, directly or indirectly, into heat.

Copper losses, also referred to as ohmic losses, this kind of loss is related to the resistance in the windings and is directly related to the currents flowing in the EM. For synchronous machines, only the stator contributes to the power:

$$P_{copper} = P_{Rs} = 3R_s I_{ph}^2 \tag{16}$$

where R_s is the phase winding resistance and I_{ph} is the current flowing in each phase. For induction machines the stator term is similar, but the rotor contribution must be included:

$$P_{copper} = P_{Rs} + P_{Rr} = 3R_s I_{ph}^2 + 3R_r I_r^2 \tag{17}$$

Iron losses are related to the electromagnetic fluxes passing through the ferromagnetic materials. There are two main mechanisms, namely, hysteresis and eddy currents. The power related to the hysteresis P_{hys} follows the expression:

$$P_{hys} = C_{hys} \cdot B^2 \cdot f \tag{18}$$

being proportional to the EM frequency f and with the square of the flux intensity B and the constant C_{hys} that encompasses the material specific behavior.

Regarding the eddy currents, an expression to estimate the eddy currents' dissipated power is:

$$P_{eddy} = C_{eddy} \cdot B^2 \cdot f^2 \tag{19}$$

Usually hysteresis effects, eddy currents' dissipated power, and other secondary loss mechanisms associated with magnetic flow are experimentally determined and represented by the Steinmetz equation that sums up the effect with three coefficients k, m and n to fit the EM response [71]:

$$P_{iron} = k \cdot V_c \cdot f^m \cdot B^n \tag{20}$$

Aerodynamic losses (or windage losses) represent the mechanical power dissipation due to the interaction of the EM rotor and the air gap between the rotor and stator. This phenomenon is highly dependent on the shape of the rotor and stator in the surfaces close to the air gap, and also to the rotation velocity. In the case of a cylindrical shape (very common for EMs) the coefficient C_{aero} shall be proportional to the air density ρ, to the radius r of the rotor to the power of four, and to the length of the rotor L:

$$P_{windage} = C_{aero} \cdot \omega^3 \rightarrow C_{aero} \propto \rho,\ r^4,\ L \tag{21}$$

Friction losses are a second type of mechanical loss, due to the friction occurring in the mechanical interfaces of the motor, the most important of which occurs in the bearings. Neglecting other contributions due to gaskets or other sealing components, the bearing friction can be calculated using the methodologies suggested by the manufacturers, such as:

$$\begin{cases} T_{bearing} = \frac{1}{2}\mu d P \\ P = X k_r F_r + Y k_a F_a \end{cases} \tag{22}$$

where μ is the friction coefficient determined by the type of bearing, d is the bearing diameter, X and Y are the radial and axial load factors (informed by the manufacturer), k_r and k_a are the dynamic load related to the operation conditions, and F_r and F_a are the loads acting on the bearing in the radial and axial directions.

In practice, instead of computing all the single contributions to the EM power loss, the most widespread form to represent them is by using a lumped model in which the iron losses, windage losses and friction losses are put together after an experimental evaluation. Another interesting approach that can be followed to estimate the EM losses, following a similar theoretical modeling of the single contributions is found in [72], where a strategy of scaling is used to translate a reference efficiency map into an unknown new map from a single-point analysis.

In **batteries**, there are two main mechanisms of heat generation: internal resistance and chemical reactions.

- **Internal resistance**: with the current flows in the battery pack, it is possible to determine the resistance contribution to the total energy loss and consequent heat generation. In the case of a constant current discharge, the heat generated can be expressed as:

$$Q_{batt} = (u_{OC} - u_b) \cdot i_b \tag{23}$$

Using the more general approach of the Thévenin equivalent circuit to represent the battery cells (and by extension the modules/pack) it can be determined that the heat generated in the batteries follows:

$$Q_{batt} = R_0 i_b^2 + R_1 i_1^2 + R_2 i_2^2 \tag{24}$$

- **Chemical reactions:** as is known, during the release or absorption of energy from/to the battery, chemical reactions take place. Apart from the electric equilibrium that represents the main mechanism of the chemical battery, these reactions also play a role in terms of heat generation. The heat associated with the chemical reaction can be derived by:

$$Q_{chem} = T \cdot \Delta S \frac{I}{-1 \cdot F} \rightarrow \Delta S = -1 \cdot F \frac{\partial u_b}{\partial T} \tag{25}$$

where Q_{chem} represents the heat related to the chemical reaction, T is the temperature, ΔS the entropy variation, I the current, F is the Faraday constant and u_b is the voltage.

Note that the direction is opposite in charge and discharge, so the heat generation will follow, making it exothermic during discharge and endothermic during charge, differently from the resistance heat, always increasing temperature of the cell in both directions.

Very complex models can be put in place to estimate the heat generation in the **inverter**. A possible approach is to divide the losses between switching losses and ohmic losses due to currents flowing in the circuit. For the purposes of this work, the detailed functioning of the inverter is out of scope, and its modeling is limited to its overall efficiency under the observed conditions.

To be more precise on the effects of the inverter efficiency on the powertrain output power and on the heat generation, it is possible to substitute the fixed efficiency η_{inv} with a fixed value for each quadrant of operation (forward/backward vs. accelerating/braking), or even creating a look-up table with discretized values of efficiency, whenever these values are available.

Once the various heat sources are known and modeled, it is essential to understand how this heat flows across the components of the E-PWT, how its exchange influences the temperature of the parts, and, finally, how much of the heat is extracted by the cooling system and dissipated by the ambient air.

The modeling strategy chosen to tackle the heat transfer problem is the so-called circuit equivalence model (Figure 4).

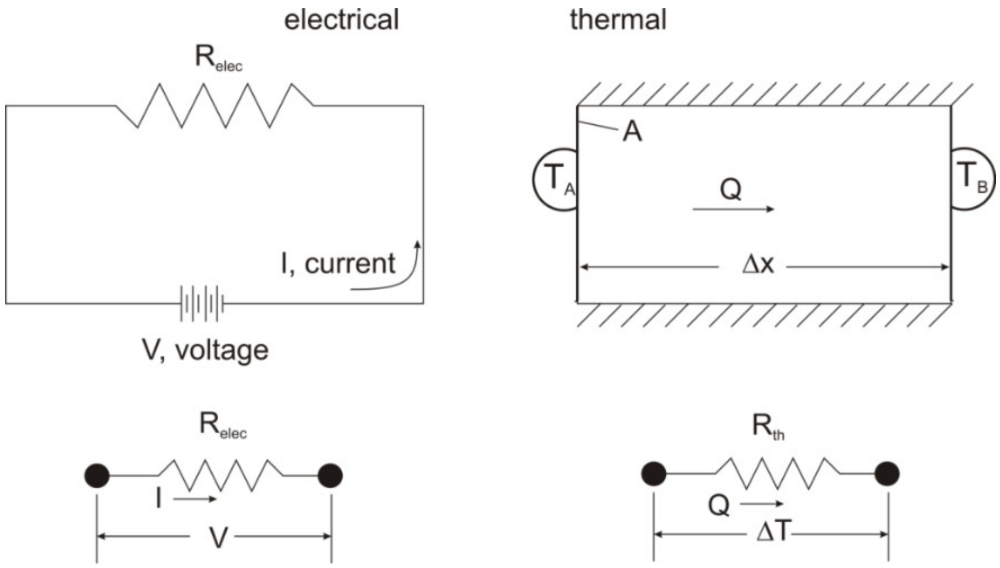

Figure 4. Thermal–electric equivalence [73].

Taking advantage of this strategy, the thermal values are compared to electric equivalents, in order to describe the system response: The current I on the electric system is equivalent to the heat transfer Q; the temperature difference between two bodies ΔT is compared to the voltage; and the electric resistance R_{elec} becomes a thermal resistance R_{th}. By using this analogy, the basic heat transfer phenomena of conduction and convection can be uniformly modeled as the equation:

$$Q = \frac{\Delta T}{R_{th}} \tag{26}$$

The main difference between each specific heat transfer condition will lay, therefore, in the strategy used to calculate the value of R_{th}. The complexity related to geometry is then removed from the main equation and passed on to its inherent coefficient.

3. The PerfECT Design Tool Implementation

3.1. The Four-Level Concept

The key concept of the developed methodology is the modularity of each of the four design steps. Each of the four levels proposed has increasing complexity and considers different phases of the product development, always regarding the concept and initial design stage. The four levels are: **Perf**ormance, **E**nergy, **C**urrents and **T**emperature (thus composing the acronym PerfECT). The levels were derived from an analysis of the natural order of the development of vehicles. In detail:

- **Performance level**: this level reflects the very beginning of the conceptual study of the vehicle, in which the only readily available information and "fixed" features are the ones decided in the requirements definition and registered in the product requirement document. This stage then focuses on the "reality check" of the desired performance, an evaluation of possible layouts for the powertrain, and a first broad procurement phase on E-PWT components, more specifically at this stage in terms of electric machines. It naturally follows that, in such an analysis, only the very essential vehicle parameters can be requested, and only very simple outcomes can be reliably expected;
- **Energy level**: as with the previous step, the energy level proposes a simple and quick modeling structure, focusing on the longitudinal dynamics response of the vehicle and adding information regarding the energy flow. When it comes to energy evaluation, the main additional information provided to the system are the curves of the e-motors (usually available from suppliers' datasheet) and information regarding battery capacity, energy management and the regenerative braking strategy. From this analysis, it is possible to extract some vital features for EVs, such as their expected range, and therefore also adjust parameters to increase/optimize them;
- **Currents level**: the gap between the energy level and currents level is probably the widest among the sequences; in order to successfully evaluate currents flowing in the high-voltage circuits of an E-PWT, it is necessary to significantly increase the complexity of the electric machine modeling and their correlated components. From this level on, the lateral dynamics simulation platform is also optionally integrated, in such a way that the designer can expand the analysis from pure drivability to include handling and stability analyses;
- **Temperature level**: as the final stage of the concept phase in product development, this level adds an important number of parameters to the analysis related to thermal characteristics. To correctly evaluate the temperature variations on the vehicle components, it is essential to understand the heat generation, heat transfer, and cooling loop features; each one of these is based on several hypotheses and parameters. The goal of the tool is not to substitute specialized thermal modeling software; therefore, a geometry-less approach was used in which the physical disposition and connections among parts is represented by lumped thermal exchange resistances. This approach allows for the PerfECT tool to be used as a target-setting instrument and as an interface with detailed CFD and multi-physics analysis.

It is evident that the use of the design tool does not encompass all the technical challenges and disciplines in vehicle development. The PerfECT design tool alone does not tackle aspects solely related to vehicle dynamics (such as suspension design), or the many other design aspects related to structural analysis, NVH, external aerodynamics, etc.

3.2. Performance Level

Figure 5 shows the main interface of the model and relevant input parameters.

At this level, it is possible to choose the speed profile and slope value/map to be followed, at the left-hand side. Then, the main block "Cycle and vehicle model" encompasses both the driver action and vehicle longitudinal response. The outputs are motor speed, motor torque, and wheel torque. The other blocks use the data to create suitable plots and output all relevant quantities, such as vehicle speed, EM power, resistive power, distance, and wheel/EM torques. Figure 6 shows the subsystem.

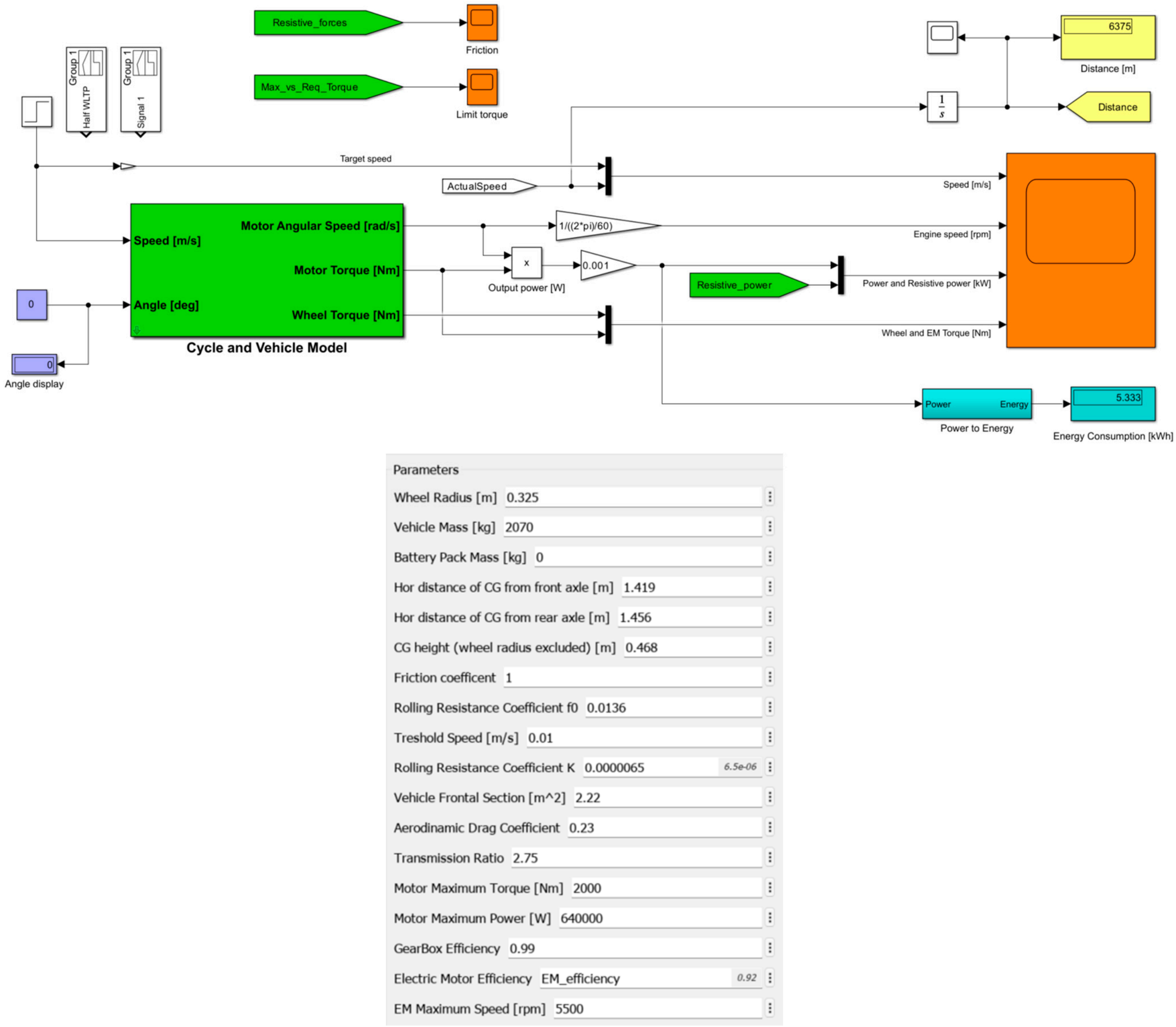

Parameters

Wheel Radius [m] 0.325

Vehicle Mass [kg] 2070

Battery Pack Mass [kg] 0

Hor distance of CG from front axle [m] 1.419

Hor distance of CG from rear axle [m] 1.456

CG height (wheel radius excluded) [m] 0.468

Friction coefficent 1

Rolling Resistance Coefficient f0 0.0136

Treshold Speed [m/s] 0.01

Rolling Resistance Coefficient K 0.0000065 6.5e-06

Vehicle Frontal Section [m^2] 2.22

Aerodinamic Drag Coefficient 0.23

Transmission Ratio 2.75

Motor Maximum Torque [Nm] 2000

Motor Maximum Power [W] 640000

GearBox Efficiency 0.99

Electric Motor Efficiency EM_efficiency 0.92

EM Maximum Speed [rpm] 5500

Figure 5. Performance level: main Simulink model view (**top**) and parameter input mask (**bottom**).

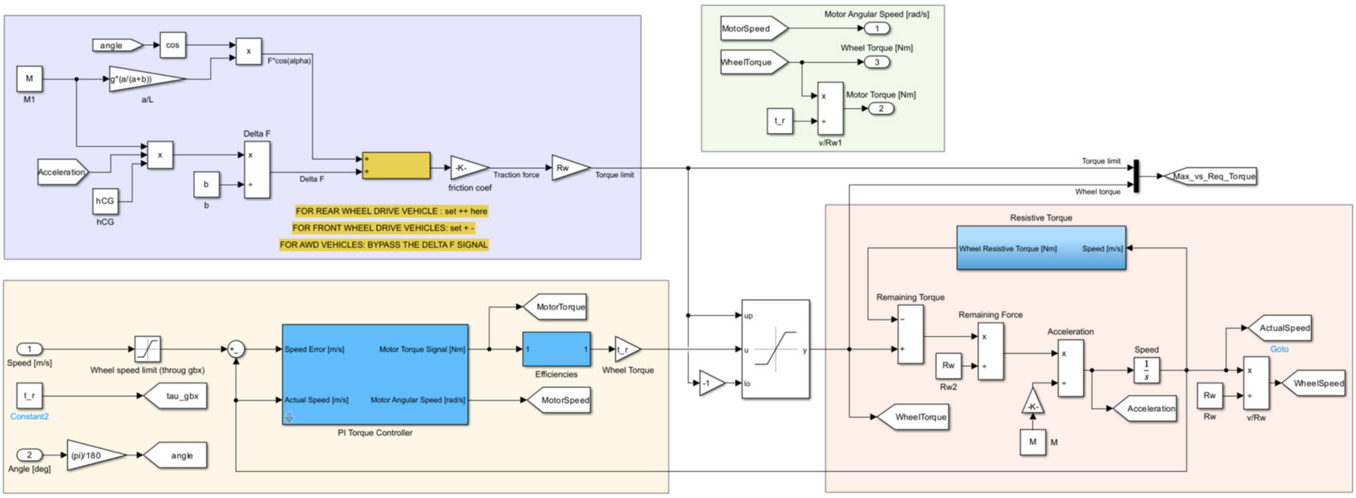

Figure 6. Performance level: cycle and vehicle model.

This level comprises four main areas:

- **Blue**: calculates the maximum traction that the tires can transmit to the road due to the friction coefficient, mass, slope, and longitudinal load transfer (h_{CG} and acceleration);
- **Yellow**: compares the actual speed and the target in the desired profile and chooses the adequate wheel torque request using a PI controller;
- **Red:** receives the saturated torque request and calculates the resistive torque based on the vehicle speed, thereby obtaining the residual acceleration, and integrating it to obtain the next timestep velocity;
- **Green:** recalls and calculates the block outputs—motor angular speed, wheel torque and motor torque.

The presented blocks sum up the main features of the "Performance" level. Using this model, it is possible to perform some analysis:

- **WOT acceleration**: by imposing a very high target velocity from the beginning of the simulation, it is possible to determine the time evolution of speed under maximum torque request. The acceleration is limited by EM features, friction, inertia, and resistive forces, which can be tuned and tweaked to achieve design goals as 0–100 km/h time;
- **Maximum slope**: by interactively increasing the slope angle input, it is possible to analyze the vehicle response on design criteria such as maximum gradeability or minimum speed/acceleration in pre-determined slope conditions;
- **Maximum speed**: it is possible to numerically determine the maximum speed achievable by the vehicle. Like the WOT analysis, it can be done by setting a high value of target speed and forcing the system to give all available power/torque in such a way that the speed will tend to the maximum obtainable value. The limit can be due to torque/power of the EM being counterposed by the resistances or due to a motor speed limit;
- **Residual acceleration:** at any given operation point, the system can be used to evaluate the total resistive power and compare it with the peak values of the powertrain to determine the available residual power that can be exploited for acceleration.

3.3. Energy Level

The second level of the analysis is very similar to the previous in terms of the layout of the simulation model. As a matter of fact, the main difference is found in the input strategy of the EM features.

Instead of inputting maximum torque and maximum power as fixed singular values, at the "Energy" level it is possible to include torque and power curves. The method used to permit such inputs is the use of Look-Up Tables (LUT). By translating the power and torque curves into discretized tables, the LUT blocks in Simulink 2023aallow for the interpolation of intermediate points to obtain dynamic saturation limits for the simulation.

Of course, apart from the torque and power data, the energy level requires a reference to EM efficiency. In this case, the input data for the model are in the form of discretized curves. By supplying the model with 2D tables of efficiency varying with load and speed, it is possible to dynamically consult the LUT to determine the instantaneous efficiency and, thus, estimate the real energy required to complete the vehicle mission.

Apart from the features of the EM, more detailed when input as tables, the other big difference on the "Energy" level regards the presence of the battery capacity. The model does not simulate the electric response per se, but estimates the discharge depth by scaling the total pack capacity (calculated by multiplying the cell capacity by the total number of cells) with the requested energy from the E-PWT. In this case, a new saturation is included regarding the maximum power output of the battery, that can potentially limit the acceleration and regeneration.

Finally, the last difference regards the modeling of the regenerative behavior. Once the energy outcome is decided upon, it is important to know the amount of energy to be recovered through the action of the EMs.

3.4. Currents Level

Figure 7 shows its main interface.

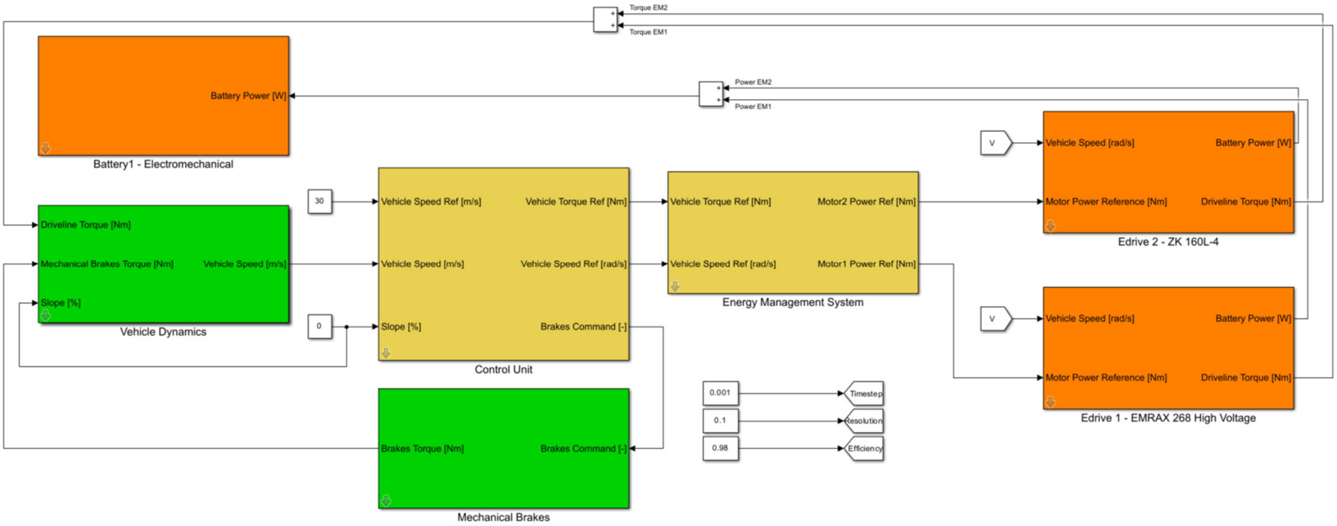

Figure 7. Currents level: main Simulink interface.

In the reported scheme, a version of the model with two independent motors is implemented, represented by the two subsystems at the right. Both blocks communicate with the Battery block (in orange at the top-left corner) by sending their power requests, and with the vehicle dynamics block by supplying the driveline torques generated. Another torque input comes from the "Mechanical Brakes" subsystem.

The vehicle dynamics block (in green at center-left position) can be used in two different modes: the first is very similar to the interfaces in the "Performance" and "Energy" levels, modeling only the longitudinal response of the vehicle through the mask's parameters; the second is where the vehicle response is simulated using the co-simulation option with VI-CRT. Apart from these "mechanical model" blocks (green) and electric model blocks (orange), two other "logic" blocks are implemented (yellow):

- **Control Unit**: this subsystem is responsible for translating the input desired speed profile and transforming it into a torque request to the E-PWT and mechanical brakes. It encompasses, basically, the PI controller and the regenerative braking controller from the "Energy" level. The main difference, in this case, is that the "Motor Torque Reference Generator", responsible for the translation of 0–100% acceleration signals into torques, considers the saturations coming from different sources. The torque limits, power limits and speed limits come from the signals in the EM models, taking into consideration not only the peak or continuous values present in the EM datasheets, but also the logic of over-torque, over-power and over-speed and their maximum allowable times;
- **Energy management system:** this subsystem is responsible for translating the total torque request coming from the controller into a torque command for each motor in the E-PWT. The first step is to perform further saturation, by inquiring the maximum power and voltage available at the battery level (Figure 8).

This procedure is conducted by means of a bisecting algorithm that iteratively predicts the necessary currents to fulfill the demand, and, using the battery data, calculates the tension drop and final power. Once this step is concluded, the torque allocation logic can be implemented.

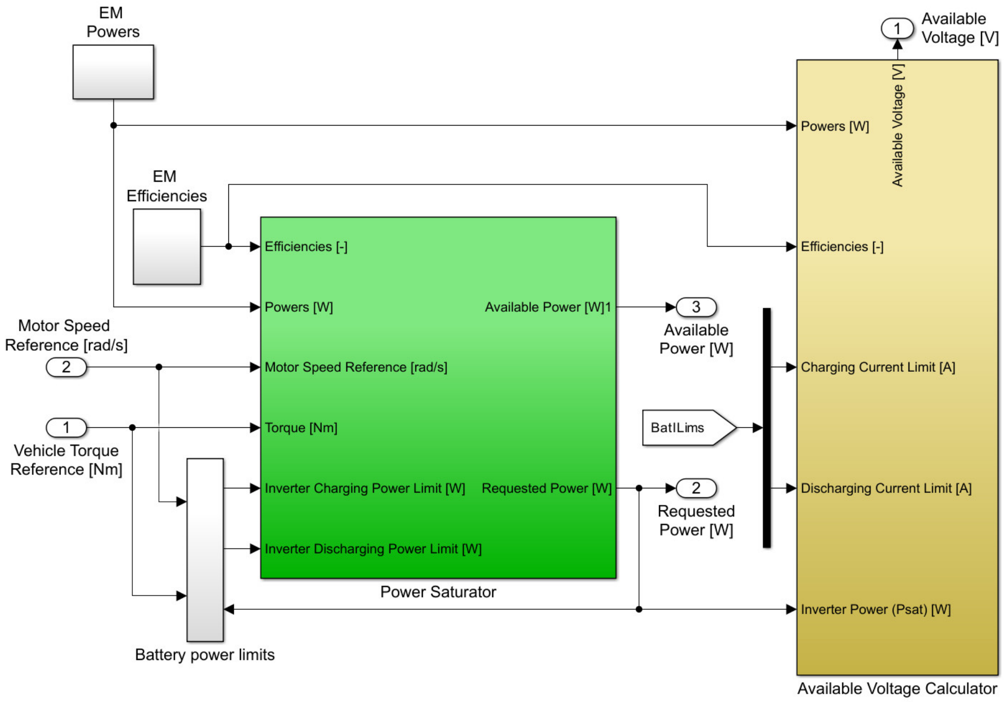

Figure 8. Currents level: energy management system.

With the physical data and MTPA maps [70], the EM blocks are responsible for transforming the torque requests into effective torque outputs and determining the currents and power necessary to do so. The main systems inside the block are:

- **Inverter**: converts the torque request into output V_d and V_q signals and motor status, after saturating the torque request with the maximum flux, available voltage, and information regarding the overloads. Using the MTPA maps this block converts reference EM torque into I_d and I_q minimum currents to achieve such torque, then through the physical model they are used to determine the voltages;
- **Overload management**: is composed of three smaller blocks, each one responsible for keeping track of one of the following key overload behaviors: Torque, Power and Speed. The overload state is characterized by an output that lies between the continuous reference and the peak reference. Obviously, it is not possible for the EM to maintain a peak performance indefinitely, so these controllers determine when to return to the continuous value after some time in overload. The method used to do so is based on a “StateFlow” module in Simulink, where an energetic approach is implemented. The basic idea is that each instant the system is over the continuous value, it is accumulating energy that will then be turned into heat and compromise long-term performance. Once the energy level is too high—based on supplier indications—StateFlow takes it back to the continuous level until the accumulated heat has not dissipated. The same outline is used for the three overload behaviors;
- **Motor electro-mechanical model**: this block is a straightforward implementation of the equivalent circuit equations in the d-q axis EM model. From them, the real output torque can be calculated, modeling the internal fluxes and EM dynamics. The electromagnetic power needed to perform this operating point load can also be determined;
- **Driveline**: the last block determines the share of the power that shall not be available to create useful mechanical torque, due to internal losses and inefficiencies (as well as the extra power requested to the storage system). Here, the copper losses, iron losses, bearing losses, aerodynamic losses, and inertial counter-torque are estimated.

Regarding the battery simulation, the main block is the “Battery pack”, where the Thévenin equivalent circuit model equations are implemented and solved, then the battery current and voltage is determined for that power level.

The current then is inputted in the “SOC Estimator” that implements a Coulomb counting strategy to determine the depth of discharge imposed and therefore integrate it to define the new SOC. The SOC level will, in the next time step, define the internal battery parameters and change the features of the equivalent circuit itself.

The third block in this subsystem regards the BMS. Keeping in mind that the name Battery Management System can refer to much more complex systems, this block is responsible for putting the system into “Protection” mode if the minimum SOC is achieved, and to make sure the requested currents, voltages and power are compatible with the battery limitations.

3.5. Temperature Level

The last level of the PerfECT tool adds a new layer to the “currents” level, meaning that the calculations previously performed do not depend on the results obtained by thermal analysis, but are essential to their calculation. It is possible, however, to use the LUT input method to create system features that vary with the temperature, creating a full closed-loop model.

For the EM thermal analysis, each component (Stator, Rotor, Shaft, End Caps, Casing, and Internal Air in the cavity) is separately considered. Inside the blocks, each one of the thermal exchanges among these components is described by establishing a thermal resistance coefficient, as well as the setup of the mass and thermal capacity of the part. Although it is difficult to gather all the necessary data in a reliable way, this approach allows for quite a simple modeling strategy.

A similar procedure is performed to model the inverters, which are divided into sub-components (chips, baseplate, heat sink and pack’s air) and each one receives a series of parameters to describe the heat exchange and temperature variations throughout the simulation. The same exact logic is valid for the battery, where the cells, pack and internal air are modeled as independent and connected elements; the heat generated follows the previously discussed mechanisms (Equations (24) and (25)).

Apart from the exchange among components, when suitable, the part can exchange heat with the cooling fluid and with the external environment. The fluid is then circulated among the components, following the actual (or desired) physical arrangement. The cooling circuit counts with a radiator, which is responsible for the heat dissipation. It is, however, possible to avoid the modeling of the actual heat exchanger by imposing a fixed temperature for the fluid at the beginning of the loop—corresponding to a situation in which the radiator is capable of completely reducing the fluid temperature to that of the one of the environments, i.e., an ideal (or over-dimensioned) heat exchanger.

Apart from the “tricky” thermal resistances that rule the internal heat exchanges in the single parts and between components and the cooling system, some other factors must be inputted in the model:

- Ambient temperature;
- Initial temperature of each part;
- Cooling fluid volume, density and heat capacity;
- Radiator dimensions and efficiency;
- Cooling circuit flow rate and distribution among components.

It is, arguably, true that the precise definition of all the thermal features beforehand (especially without access to the design or experimental tests) is an unfeasible task; however, the “Temperature” level of the PerfECT tool presents itself as a great tool for supporting design teams when the project approaches the system design and component selection. Imagine a cooling designer that can set the targets for her heat exchangers, pumps, and the fluid itself, not by experience, trial-and-error, or by looking at benchmarking examples, but by testing the effects of each choice in the predicted temperature variations of the system.

The possibility of running sensitivity analyses and optimizations without the computational burden often associated with CFD or multi-physics software has huge potential.

4. Practical Validation on a Tesla Model 3

In this section the modelling strategy will be implemented and validated with a real-m[use case. The application in a real vehicle case study serves not only as an example, but as the basis for a well-needed experimental validation of the methodology.

4.1. The Vehicle

The vehicle chosen for the case study is the Tesla Model 3, specifically, the 2021 Tesla Model 3 Long-Range AWD. This vehicle represents one of the most popular and widespread BEVs on the market. Table 1 shows some of the basic geometric and inertial parameters of the vehicle.

Table 1. Tesla Model 3 main dimensions and mass parameters.

Parameter	Value	Unit
wheelbase	2875	mm
track	1580	mm
mass LF	517	kg
mass RF	505	kg
mass LR	530	kg
mass RR	518	kg
total mass	2070	kg
unsprung mass front	22.7	kg
unsprung mass rear	19.5	kg
sprung mass	1985.6	kg
CoG x	1419	mm
CoG y	18	mm
CoG z	468	mm
I_{xx}	2.65×10^8	$kg \times mm^2$
I_{yy}	1.04×10^9	$kg \times mm^2$
I_{zz}	1.69×10^9	$kg \times mm^2$
I_{xy}	3.22×10^6	$kg \times mm^2$
I_{xz}	4.14×10^7	$kg \times mm^2$
I_{yz}	4.15×10^5	$kg \times mm^2$

The overall dimensions and masses were easy to obtain. The inertias were estimated from reference values present in software databases [64] and scaled to match the specific model. The CoG height (Z coordinate) was harder to assess. One widespread technique, adopted in this case, is the modified reaction method (MRM) [74–76].

The aerodynamic data of the Tesla Mode 3 can be found in Table 2.

Table 2. Tesla Model 3 main aerodynamic features.

Parameter	Value	Unit
Air density	1.225	kg/m^3
Frontal area	2.22	m^2
Drag coefficient (C_x)	0.23	-
Lift coefficient (C_z)	0.09	-
CoP distribution	0.5	-

The Tesla Model 3 battery pack, more specifically the Long-Range version taken into consideration, is composed of four modules, as shown in Figure 9.

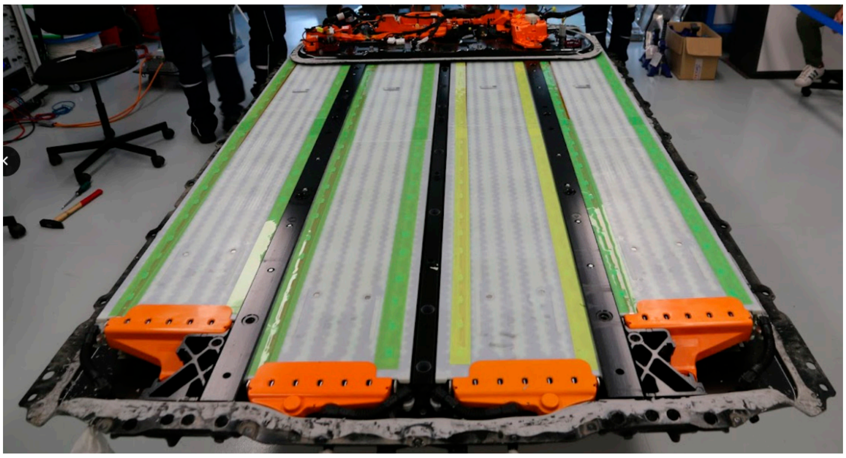

Figure 9. Tesla Model 3 unassembled battery pack.

Each of the modules is composed of cylindrical cells disposed in series and parallel. As can be seen, the two modules on the outer edges of the pack are smaller than the other two central ones. This is not only a geometric placement difference, but a change in the number of cells. As a matter of fact, the external modules are composed of 1058 cells while the internal ones have 1150 units. The cells inside the modules are organized in:

- 23 series and 46 parallel for the external modules;
- 25 series and 46 parallel for the internal modules.

The Tesla Model 3 uses the model of 21,700 of cylindrical cells, the main features of which are listed in Table 3.

Table 3. Tesla Model 3 main battery cell parameters.

Parameter	Value	Unit
Cell height	70	mm
Cell diameter	21	mm
Cell mass	68.5	g
Nominal capacity	4.80	Ah
Maximum continuous current	7.0	A
Maximum peak current	17.8	A
Energy @ C/10	17.1	Wh
Continuous power	24.0	W
Peak power	64.6	W

Regarding the Thévenin parameters, the PerfECT tool is designed to receive variable parameters according to internal states of the battery, for example: R_0, R_1, C_1, R_2 and C_2 can vary with SOC, temperature, charge/discharge direction, aging, etc. In the specific case of the Tesla Model 3, not all parameters were used, and the model was only based on the SOC (for the other dimensions the same parameter values were maintained, so no effective variations were observed). Table 4 shows the used values for each SOC level, as well as the reference open-circuit voltage for that state of charge.

Table 4. Tesla Model 3 Thévenin parameters varying with SOC.

SOC	V_{OC} [V]	R0 [Ω]	R1 [Ω]	C1 [F]	R2 [Ω]	C2 [F]
0.00	2.75	0.030	0.0064	200	0.0064	1000
0.10	2.96	0.028	0.0064	250	0.0064	2500
0.20	3.17	0.026	0.0072	750	0.0064	8500
0.30	3.33	0.027	0.0072	1100	0.0064	12,000
0.40	3.53	0.025	0.0072	1450	0.0064	10,000
0.50	3.72	0.023	0.008	1650	0.008	15,000
0.60	3.88	0.024	0.0088	1800	0.0096	21,500
0.70	3.96	0.026	0.0088	2000	0.008	15,000
0.80	4.08	0.027	0.0128	2250	0.0096	15,000
0.90	4.18	0.029	0.024	2100	0.016	22,500
1.00	4.20	0.030	0.0216	2250	0.02	30,000

The chosen Tesla Model 3 presents an interesting powertrain layout—two electric motors, front and rear, with different EM architectures—which makes the analysis more complex but allows for the study of some thought-provoking control choices and vehicle responses. The EM parameters can be found in Table 5.

Table 5. Tesla Model 3 front and rear EM main parameters.

Parameter	Value	Unit
Front motor (Induction Motor)		
Pole pairs	2	-
Max continuous current	532	A
Max peak current	940	A
Max continuous torque	172	N × m
Max peak torque	220	N × m
Max continuous power	89.77	kW
Max peak power	158.0	kW
Max rotational speed	18,000	rpm
Rotational inertia	0.1	$kg \times m^2$
Transmission ratio	9:1	-

Table 5. *Cont.*

Parameter	Value	Unit
Rear motor (Synchronous Motor)		
Pole pairs	3	-
Max continuous current	600	A
Max peak current	1000	A
Max continuous torque	315	N × m
Max peak torque	430	N × m
Max continuous power	110.0	kW
Max peak power	192.0	kW
Max rotational speed	18,000	rpm
Rotational inertia	0.1	kg × mm^2
Transmission ratio	9:1	-

4.2. Experimental Methodology

When starting the analysis of the experimental setup, it is important to define the track used during the campaign. The chose venue was the MotorOasi in the city of Susa, near Torino in northern Italy (Figure 10). These facilities are used both for vehicle testing and for driving courses, and have a series of different features, such as a low-adherence road and external disturbances with floor actuators.

Figure 10. Tesla Model 3 during the experimental campaign.

The main areas of the track used in the tests were the 300 m straight line, and the middle rim of the roundabout, with a 75 m diameter and a width of 20 m.

Environmental conditions were mild and constant, with temperatures between 23 and 28 °C, air humidity between 61 and 74% and wind speeds not exceeding 11 km/h.

Three main maneuvers were performed during the campaign: 0-100-0 accelerations, a double-lane change [77] (as per the ISO 3888-2 standard [78]), and constant-radius cornering.

The Tesla Model 3 was also chosen as the key vehicle to be analyzed because of the availability of the CAN Bus data through its DBC file, making it possible to access a myriad of internal signals present in the vehicle. Some of the most relevant signals include:

- Body accelerations in the three directions;
- Vehicle speed;
- Pitch and roll angles and velocities;
- Yaw rate;
- Steering wheel angle and speed;
- Wheel rotational speed (FL, FR, RL, RR);
- Bus high voltage (front and rear);
- Bus current (front and rear);
- Acceleration pedal position;
- Brake pedal activation signal (ON/OFF);
- ABS activation flag;
- ESP activation flag and related parameters;
- Motor torque request (front and rear);
- Motor output torque (front and rear);
- Motor output power (front and rear);
- Envelope of motor phase current (front and rear);
- Battery state of charge;
- Battery voltage;
- GPS positioning (latitude and longitude).

Apart from the listed signals, a series of other channels are accessible, describing several internal parameters of the BMS, user interface information, recharging status, ADAS/autopilot, HVAC, etc. Overall, more than 3000 different signals can be extracted from the CAN Bus reading.

Nevertheless, some signals and sensors are not present, not even in the most modern and connected vehicles such as the Tesla Model3, and this motivated further instrumentation of the track tests. The vehicle's layout with the added sensors is shown in Figure 11.

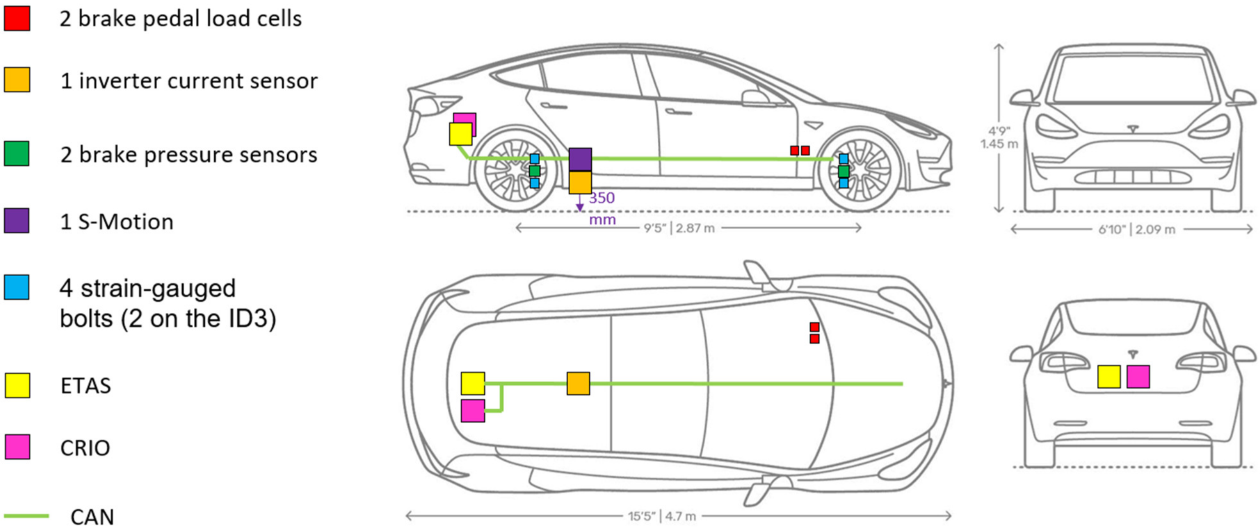

Figure 11. Tesla Model 3 sensors and datalogging layout.

Some of the sensors were installed in the vehicle for other experimental goals, such as the brake pedal load cell (used to correlate the driver braking effort with the system response) or the strain-gauged bolts, serving to test the procedure of wheel load estimation, as described in [79].

After the acquisition and logging, an important step in the analysis is the post-processing of the signals. The process, conducted in MATLAB 2023a, followed these steps [79]:

- **Validation**—verification of each signal to guarantee the coherence and magnitude regarding the physical value anticipated;
- **Data cleanse**—cancelling of missing data points, zero values and other eventual outliers or faulty signals;
- **Integration**—gathering data from the different dataloggers, ensuring the synchronization of the information;
- **Determination of the relevant maneuvers**—the acquisition begins before the actual start of the maneuver, necessitating a "cut" of the data where useful information is lacking;
- **Filtering**—in signals with high noise, low-pass filters are applied to smooth the curve and help with the data analysis and comparison.

5. Experimental Results

In this session, an extract of the main experimental results is presented, highlighting the main parameters that demonstrate the precision of the proposed methodology. More specifically, two maneuvers are presented: the straight line 0-100-0 event, with which it is possible to validate the overall longitudinal dynamics and e-powertrain electro-mechanical response; and the double-lane change, especially useful for the validation of lateral dynamics and handling.

5.1. Straight Line 0-100-0 km/h

In Figure 12, it is possible to see four of the main parameters related to the longitudinal dynamics and the electro-mechanical response related to the e-powertrain.

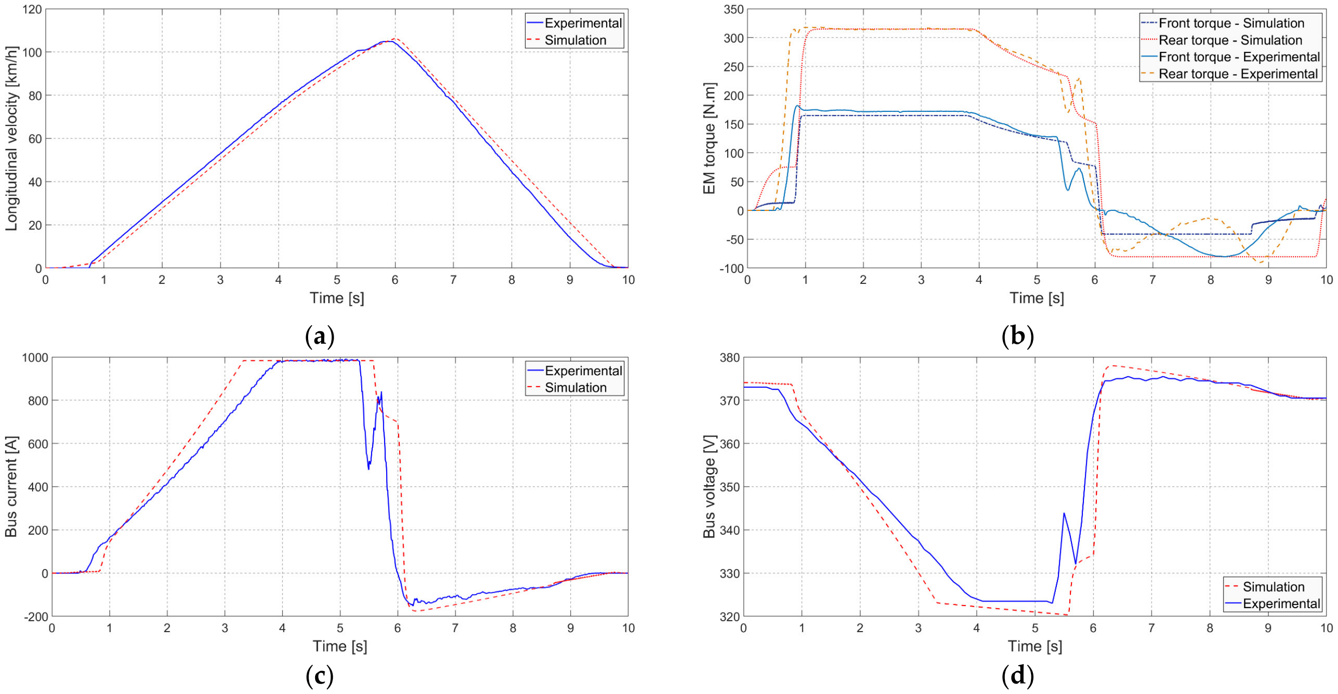

(**a**) (**b**) (**c**) (**d**)

Figure 12. Comparison between experimental and simulation data on the 0-100-0 km/h maneuver: (**a**) vehicle speed; (**b**) electric motor torque; (**c**) DC current at bus; and (**d**) bus voltage.

The experimental and simulated trends are well correlated. Both in terms of shape and magnitude, all four simulated parameters follow the observed curves obtained on the track tests.

The main difference found in the comparison of the plots in Figure 12 lies on the braking phase, from the time of 6.1 s. Indeed, the logic ruling the torque split between the front and rear motors during the regenerative braking phase was not directly tuned to reflect the behavior of the Tesla Model 3, although this operation could be performed by adjusting the "Energy Management System" shown in Figure 7.

Overall, it is possible to assert that the longitudinal response of the PerfECT design tool is sufficiently accurate in its description of the vehicle's behavior and can be effectively used as a predictive tool during the design of BEVs.

5.2. Double-Lane Change at 50 km/h

A similar analysis can be performed by looking at the DLC manoeuvre, in this case performed at a speed of 70 km/h. Four important features of the lateral dynamics are displayed in Figure 13.

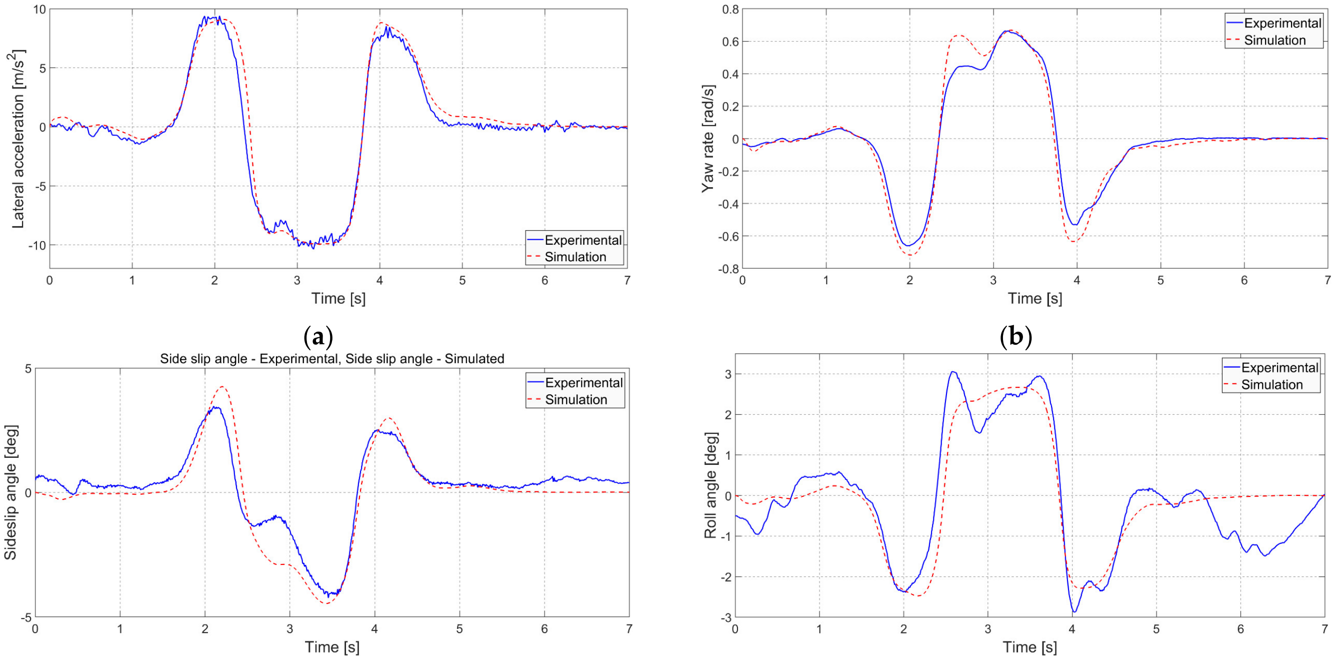

(**a**) (**b**)

(**c**) (**d**)

Figure 13. Comparison between experimental and simulation data on the double-lane-change maneuver: (**a**) lateral acceleration; (**b**) yaw rate; (**c**) side slip angle; and (**d**) roll angle.

For the virtual reproduction of the DLC maneuver, the steering angle observed in the experimental tests is hard-inputted on the virtual driver to avoid differences caused by the approach used by the human driver and the virtual driver (as is often the case). Also, in this case it is easy to notice that the proposed model closely reflects the behavior seen in the experimental tests. Apart from some residual noise coming from the experimental equipment and a slight deviation between 2.5 and 3 s of the maneuver, the overall shape of the curves and magnitude of the parameters proves to be accurate.

6. Conclusions

This article proposed a multi-step methodology for the modeling and simulation of BEVs, entitled the PerfECT Design Tool. As the name suggests, this virtual simulation method aims to provide a suitable strategy to support the early stages of the engineering design process for electric vehicles.

The article described the theoretical background and main equations used to simulate the mechanical, electrical, and thermal behavior of an EV. From this theoretical background, it was possible to build a complete model combining MATLAB/Simulink and the vehicle dynamics software VI-CRT, divided into four independent but sequential steps: Performance, Energy, Currents, and Temperature.

This model was then validated through a series of experimental maneuvers performed with a Tesla Model 3, demonstrating its accuracy. The PerfECT design tool can be used, as proposed, to help during the first stages of the new EV design and represents a contribution to the industry and academia as a comprehensive and increasingly complex solution for simulations.

Funding: This research received no external funding.

Data Availability Statement: Data are contained within the article.

Acknowledgments: The content of this article was developed in the context of the author's industrial Ph.D. program and partnership between Politecnico di Torino, CNR and Beond. Special thanks to Massimiliana Carello, Elisabetta Punta and all the team at Beond for their support during the technical and experimental activities; acknowledgements also to the VI-Grade team for the software license and technical support.

Conflicts of Interest: The author declares no conflict of interest.

References

1. Automobile—Early Electric Automobiles | Britannica. March 2023. Available online: https://www.britannica.com/technology/automobile/Early-electric-automobiles (accessed on 29 November 2023).
2. What Was the Henney Kilowatt? 2018. Available online: https://blog.consumerguide.com/what-was-the-henney-kilowatt/ (accessed on 29 November 2023).
3. Shahan, Z. Electric Car History (In Depth). 2015. Available online: https://cleantechnica.com/2015/04/26/electric-car-history/ (accessed on 29 November 2023).
4. Zero-Emission Vehicle Program | California Air Resources Board. March 2023. Available online: https://ww2.arb.ca.gov/our-work/programs/zero-emission-vehicle-program/about (accessed on 29 November 2023).
5. Berdichevsky, G.; Kelty, K.; Straubel, J.; Toomre, E. *The Tesla Roadster Battery System*; Tesla Motors: Austin, TX, USA, 2006.
6. Blomgren, G.E. The Development and Future of Lithium Ion Batteries. *J. Electrochem. Soc.* **2016**, *164*, A5019. [CrossRef]
7. EEC. Council Directive 91/441/EEC of 26 June 1991 amending Directive 70/220/EEC on the approximation of the laws of the Member States relating to measures to be taken against air pollution by emissions from motor vehicles. *Off. J. L* **1991**, *242*, 1–106.
8. Q&A: Commission Proposal on the New Euro 7 Standards, Text. March 2023. Available online: https://ec.europa.eu/commission/presscorner/detail/en/qanda_22_6496 (accessed on 29 November 2023).
9. Fit for 55: Zero CO_2 Emissions for New Cars and Vans in 2035 | News | European Parliament. 2023. Available online: https://www.europarl.europa.eu/news/en/press-room/20230210IPR74715/fit-for-55-zero-co2-emissions-for-new-cars-and-vans-in-2035 (accessed on 29 November 2023).
10. Deal Confirms Zero-Emissions Target for New Cars and Vans in 2035 | News | European Parliament. 2022. Available online: https://www.europarl.europa.eu/news/en/press-room/20221024IPR45734/deal-confirms-zero-emissions-target-for-new-cars-and-vans-in-2035 (accessed on 29 November 2023).
11. Frith, J.T.; Lacey, M.J.; Ulissi, U. A non-academic perspective on the future of lithium-based batteries. *Nat. Commun.* **2023**, *14*, 420. [CrossRef]
12. Electric Vehicles—Worldwide | Statista Market Forecast. March 2023. Available online: https://www.statista.com/outlook/mmo/electric-vehicles/worldwide (accessed on 29 November 2023).
13. Electric Vehicle Market Share, Size, Analysis | EV Market Growth. March 2023. Available online: https://www.alliedmarketresearch.com/electric-vehicle-market (accessed on 29 November 2023).
14. Battery Recycling Policies for Boosting Electric Vehicle Adoption: Evidence from a Choice Experimental Survey. March 2023. Available online: https://www.springerprofessional.de/en/battery-recycling-policies-for-boosting-electric-vehicle-adoptio/23137392 (accessed on 29 November 2023).
15. Nong, G.P.; Pang, S.L. Research on the Electric Vehicle Remanufacturable Battery Supply Chain with Recycling Channels. *Adv. Mater. Res.* **2013**, *773*, 948–953. [CrossRef]
16. Feng, S. System dynamics model for battery recycling of electric vehicles in Anylogic simulation. *Int. J. Internet Manuf. Serv.* **2018**, *5*, 405–418. [CrossRef]
17. Hao, F.; Lu, X.; Qiao, Y.; Chen, X. Crashworthiness Analysis of Electric Vehicle with Energy-Absorbing Battery Modules. *J. Eng. Mater. Technol.* **2017**, *139*, 021022. [CrossRef]
18. Kang, S.; Kwon, M.; Yoon Choi, J.; Choi, S. Full-scale fire testing of battery electric vehicles. *Appl. Energy* **2023**, *332*, 120497. [CrossRef]
19. Kim, S.; Lee, J.; Lee, C. Does Driving Range of Electric Vehicles Influence Electric Vehicle Adoption? *Sustainability* **2017**, *9*, 1783. [CrossRef]
20. Kumar, L.; Ravi, N. Electric vehicle charging method and impact of charging and discharging on distribution system: A review. *Int. J. Electr. Hybrid Veh.* **2022**, *14*, 87–111. [CrossRef]

21. Dong, J.; Lin, Z. Within-day recharge of plug-in hybrid electric vehicles: Energy impact of public charging infrastructure. *Transp. Res. Part Transp. Environ.* **2012**, *17*, 405–412. [CrossRef]
22. Gruber, P.W.; Medina, P.A.; Keoleian, G.A.; Kesler, S.E.; Everson, M.P.; Wallington, T.J. Global Lithium Availability. *J. Ind. Ecol.* **2011**, *15*, 760–775. [CrossRef]
23. Ahmed, S.; Nelson, P.A.; Gallagher, K.G.; Susarla, N.; Dees, D.W. Cost and energy demand of producing nickel manganese cobalt cathode material for lithium ion batteries. *J. Power Sources* **2017**, *342*, 733–740. [CrossRef]
24. Rieck, F.; Machielse, K.; van Duin, R. Will Automotive Be the Future of Mobility? Striving for Six Zeros. *World Electr. Veh. J.* **2020**, *11*, 10. [CrossRef]
25. Girardi, P.; Gargiulo, A.; Brambilla, P.C. A comparative LCA of an electric vehicle and an internal combustion engine vehicle using the appropriate power mix: The Italian case study. *Int. J. Life Cycle Assess.* **2015**, *20*, 1127–1142. [CrossRef]
26. Eshetu, G.G.; Zhang, H.; Judez, X.; Adenusi, H.; Armand, M.; Passerini, S.; Figgemeier, E. Production of high-energy Li-ion batteries comprising silicon-containing anodes and insertion-type cathodes. *Nat. Commun.* **2021**, *12*, 5459. [CrossRef]
27. Varzi, A.; Raccichini, R.; Passerini, S.; Scrosati, B. Challenges and prospects of the role of solid electrolytes in the revitalization of lithium metal batteries. *J. Mater. Chem. A* **2016**, *4*, 17251–17259. [CrossRef]
28. Braga, M.H.; Grundish, N.S.; Murchison, A.J.; Goodenough, J.B. Alternative strategy for a safe rechargeable battery. *Energy Environ. Sci.* **2017**, *10*, 331–336. [CrossRef]
29. Rizzello, A.; Scavuzzo, S.; Ferraris, A.; Airale, A.G.; Carello, M. Temperature-Dependent Thévenin Model of a Li-Ion Battery for Automotive Management and Control. In Proceedings of the 2020 IEEE International Conference on Environment and Electrical Engineering and 2020 IEEE Industrial and Commercial Power Systems Europe (EEEIC/I&CPS Europe), Madrid, Spain, 9–12 June 2020; IEEE: Madrid, Spain, 2020; pp. 1–6, ISBN 978-1-72817-455-6. [CrossRef]
30. Rizzello, A.; Scavuzzo, S.; Ferraris, A.; Airale, A.G.; Bianco, E.; Carello, M. Non-linear Kalman Filters for Battery State of Charge Estimation and Control. In Proceedings of the 2021 International Conference on Electrical, Computer, Communications and Mechatronics Engineering (ICECCME), Piscataway, NJ, USA, 7–8 October 2021; pp. 1–7. [CrossRef]
31. Christensen, J.; Albertus, P.; Sanchez-Carrera, R.S.; Lohmann, T.; Kozinsky, B.; Liedtke, R.; Ahmed, J.; Kojic, A. A Critical Review of Li/Air Batteries. *J. Electrochem. Soc.* **2011**, *159*, R1–R30. [CrossRef]
32. Wang, H.; Yang, Y.; Liang, Y.; Robinson, J.T.; Li, Y.; Jackson, A.; Cui, Y.; Dai, H. Graphene-Wrapped Sulfur Particles as a Rechargeable Lithium–Sulfur Battery Cathode Material with High Capacity and Cycling Stability. *Nano Lett.* **2011**, *11*, 2644–2647. [CrossRef]
33. Ji, X.; Lee, K.T.; Nazar, L.F. A highly ordered nanostructured carbon–sulphur cathode for lithium–sulphur batteries. *Nat. Mater.* **2009**, *8*, 500–506. [CrossRef]
34. Hartmann, P.; Bender, C.L.; Sann, J.; Dürr, A.K.; Jansen, M.; Janek, J.; Adelhelm, P. A comprehensive study on the cell chemistry of the sodium superoxide (NaO_2) battery. *Phys. Chem. Chem. Phys.* **2013**, *15*, 11661–11672. [CrossRef]
35. Hartmann, P.; Bender, C.L.; Vračar, M.; Dürr, A.K.; Garsuch, A.; Janek, J.; Adelhelm, P. A rechargeable room-temperature sodium superoxide (NaO_2) battery. *Nat. Mater.* **2013**, *12*, 228–232. [CrossRef] [PubMed]
36. All-Solid-State Lithium-Ion Batteries. March 2023. Available online: https://www.hitachizosen.co.jp/english/business/field/functional/as-lib.html (accessed on 29 November 2023).
37. Duan, Y.; Bai, X.; Yu, T.; Rong, Y.; Wu, Y.; Wang, X.; Yang, J.; Wang, J. Research progress and prospect in typical sulfide solid-state electrolytes. *J. Energy Storage* **2022**, *55*, 105382. [CrossRef]
38. Suzuki, N.; Watanabe, T.; Fujiki, S.; Aihara, Y. Solid-State Batteries with Inorganic Electrolytes. In *Encyclopedia of Electrochemistry*; John Wiley & Sons, Ltd.: Hoboken, NJ, USA, 2020; pp. 1–62; ISBN 978-3-527-61042-6. [CrossRef]
39. Carello, M.; Pinheiro, H.D.C.; Longega, L.; Di Napoli, L. Design and Modelling of the Powertrain of a Hybrid Fuel Cell Electric Vehicle. *SAE Int. J. Adv. Curr. Pract. Mobil.* **2021**, *3*, 2878–2892. [CrossRef]
40. Bianco, E.; Di Napoli, L.; Grano, E.; Carello, M. E-scooter Modelling: Battery and Fuel Cell System Integration. In *Advances in Italian Mechanism Science*; Niola, V., Gasparetto, A., Quaglia, G., Carbone, G., Eds.; Springer International Publishing: Cham, Switzerland, 2022; pp. 909–916; ISBN 978-3-031-10776-4. [CrossRef]
41. Bianco, E.; Carello, M. A first e-scooter powertrain analysis for Fuel Cell integration. In Proceedings of the 2022 International Conference on Electrical, Computer, Communications and Mechatronics Engineering (ICECCME), Maldives, Maldives, 16–18 November 2022; pp. 1–6. [CrossRef]
42. Messana, A.; Airale, A.G.; Ferraris, A.; Sisca, L.; Carello, M. Correlation between thermo-mechanical properties and chemical composition of aged thermoplastic and thermosetting fiber reinforced plastic materials: Korrelation zwischen thermomechanischen Eigenschaften und chemischer Zusammensetzung von gealterten thermo- und duroplastischen faserverstärkten Kunst. *Mater. Werkst.* **2017**, *48*, 447–455. [CrossRef]
43. Messana, A.; Sisca, L.; Ferraris, A.; Airale, A.G.; Pinheiro, H.d.C.; Sanfilippo, P.; Carello, M. From Design to Manufacture of a Carbon Fiber Monocoque for a Three-Wheeler Vehicle Prototype. *Materials* **2019**, *12*, 332. [CrossRef]
44. Airale, A.; Carello, M.; Ferraris, A.; Sisca, L. Moisture effect on mechanical properties of polymeric composite materials. *AIP Conf. Proc.* **2016**, *1736*, 020020. [CrossRef]
45. Carello, M.; Airale, A.G.; Ferraris, A.; Messana, A.; Sisca, L. Static Design and Finite Element Analysis of Innovative CFRP Transverse Leaf Spring. *Appl. Compos. Mater.* **2017**, *24*, 1493–1508. [CrossRef]

46. Sisca, L.; Locatelli Quacchia, P.T.; Messana, A.; Airale, A.G.; Ferraris, A.; Carello, M.; Monti, M.; Palenzona, M.; Romeo, A.; Liebold, C.; et al. Validation of a Simulation Methodology for Thermoplastic and Thermosetting Composite Materials Considering the Effect of Forming Process on the Structural Performance. *Polymers* **2020**, *12*, 2801. [CrossRef]
47. Carello, M.; Pinheiro, H.d.C.; Messana, A.; Freedman, A.; Ferraris, A.; Airale, A.G. Composite Control Arm Design: A Comprehensive Workflow. *SAE Int. J. Adv. Curr. Pract. Mobil.* **2021**, *3*, 2355–2369. [CrossRef]
48. Fasana, A.; Ferraris, A.; Airale, A.G.; Berti Polato, D.; Carello, M. Experimental Characterization of Damped CFRP Materials with an Application to a Lightweight Car Door. *Shock Vib.* **2017**, *2017*, 7129058. [CrossRef]
49. Carello, M.; Airale, A.G. Composite Suspension Arm Optimization for the City Vehicle XAM 2.0. In *Design and Computation of Modern Engineering Materials*; Öchsner, A., Altenbach, H., Eds.; Springer International Publishing: Cham, Switzerland, 2014; pp. 257–272; ISBN 978-3-319-07382-8. [CrossRef]
50. Cubito, C.; Rolando, L.; Ferraris, A.; Carello, M.; Millo, F. Design of the Control Strategy for a Range Extended Hybrid Vehicle by means of Dynamic Programming Optimization. In Proceedings of the 2017 IEEE Intelligent Vehicles Symposium (IV), Los Angeles, USA, 11–14 June 2017; pp. 1234–1241. [CrossRef]
51. Ferraris, A.; De Cupis, D.; De Carvalho Pinheiro, H.; Messana, A.; Sisca, L.; Airale, A.G.; Carello, M. *Integrated Design and Control of Active Aerodynamic Features for High Performance Electric Vehicles*; SAE Technical Paper 2020-36-0079; SAE International: Warrendale, PA, USA, 2021. [CrossRef]
52. Brusaglino, G.; Buja, G.; Carello, M.; Carlucci, A.P.; Onder, C.H.; Razzetti, M. New technologies demonstrated at Formula Electric and Hybrid Italy 2008. *World Electr. Veh. J.* **2009**, *3*, 160–171. [CrossRef]
53. Liu, B.; Zhang, H.; Zhu, S. An Incremental V-Model Process for Automotive Development. In Proceedings of the 2016 23rd Asia-Pacific Software Engineering Conference (APSEC), Hamilton, New Zealand, 6–9 December 2016; pp. 225–232. [CrossRef]
54. Castellanos Molina, L.M.; Manca, R.; Hegde, S.; Amati, N.; Tonoli, A. Predictive handling limits monitoring and agility improvement with torque vectoring on a rear in-wheel drive electric vehicle. *Veh. Syst. Dyn.* **2023**, 1–25. [CrossRef]
55. Pinheiro, H.d.C.; Punta, E.; Carello, M.; Ferraris, A.; Airale, A.G. Torque Vectoring in Hybrid Vehicles with In-Wheel Electric Motors: Comparing SMC and PID control. In Proceedings of the 2021 IEEE International Conference on Environment and Electrical Engineering and 2021 IEEE Industrial and Commercial Power Systems Europe (EEEIC/I CPS Europe), Bari, Italy, 7–10 September 2021; pp. 1–6. [CrossRef]
56. Tramacere, E.; Castellanos, L.M.M.; Amati, N.; Tonoli, A.; Bonfitto, A. Adaptive LQR Control for a Rear-Wheel Steering Battery Electric Vehicle. In Proceedings of the 2022 IEEE Vehicle Power and Propulsion Conference (VPPC), Merced, CA, USA, 1–4 November 2022; pp. 1–6. [CrossRef]
57. De Carvalho Pinheiro, H.; Carello, M. Design and Validation of a High-Level Controller for Automotive Active Systems. *SAE Int. J. Veh. Dyn. Stab. NVH* **2023**, *7*, 83–98. [CrossRef]
58. Vošahlík, D.; Haniš, T. Traction Control Allocation Employing Vehicle Motion Feedback Controller for Four-Wheel-Independent-Drive Vehicle. *IEEE Trans. Intell. Transp. Syst.* **2023**, *24*, 14570–14579. [CrossRef]
59. Carello, M.; Ferraris, A.; Pinheiro, H.d.C.; Stanke, D.C.; Gabiati, G.; Camuffo, I.; Grillo, M. Human-Driving Highway Overtake and Its Perceived Comfort: Correlational Study Using Data Fusion. In Proceedings of the WCX SAE World Congress Experience, Detroit, MI, USA, 21–23 April 2020. SAE Technical Paper 2020-01-1036. [CrossRef]
60. Pinheiro, H.d.C.; Stanke, D.C.; Ferraris, A.; Carello, M.; Gabiati, G.; Camuffo, I.; Grillo, M. Autonomous Driving Scenario Generation in Overtake Manoeuvres Through Data Fusion. In *Advances in Italian Mechanism Science*; Niola, V., Gasparetto, A., Eds.; Springer: Berlin/Heidelberg, Germany, 2021; pp. 786–794; ISBN 978-3-030-55807-9. [CrossRef]
61. Milliken, W.F. *Race Car Vehicle Dynamics*; Society of Automotive Engineers: Warrendale, PA, USA, 1995; ISBN 978-0-7680-0103-7.
62. Pinheiro, H.d.C.; Carello, M.; Punta, E. Torque Vectoring Control Strategies Comparison for Hybrid Vehicles with Two Rear Electric Motors. *Appl. Sci.* **2023**, *13*, 8109. [CrossRef]
63. Genta, G.; Morello, L. *The Automotive Chassis*; Springer Science & Business Media: Berlin/Heidelberg, Germany, 2008; Volume 1–2, ISBN 978-1-4020-8676-2.
64. VI-grade GmbH. *VI-CarRealTime 20.0 Documentation*; VI-grade GmbH: Darmstadt, Germany, 2020.
65. Ydrefors, L.; Hjort, M.; Kharrazi, S.; Jerrelind, J.; Stensson Trigell, A. Rolling resistance and its relation to operating conditions: A literature review. *Proc. Inst. Mech. Eng. Part J. Automob. Eng.* **2021**, *235*, 2931–2948. [CrossRef]
66. Nicoletti, L.; Mayer, S.; Brönner, M.; Schockenhoff, F.; Lienkamp, M. Design Parameters for the Early Development Phase of Battery Electric Vehicles. *World Electr. Veh. J.* **2020**, *11*, 47. [CrossRef]
67. Electric Powertrain: Energy Systems, Power Electronics and Drives for Hybrid, Electric and Fuel Cell Vehicles | Wiley. April 2023. Available online: https://www.wiley.com/en-au/Electric+Powertrain%253A+Energy+Systems%252C+Power+Electronics+and+Drives+for+Hybrid%252C+Electric+and+Fuel+Cell+Vehicles-p-9781119063643 (accessed on 29 November 2023).
68. Krishnan, R. *Electric Motor Drives: Modeling, Analysis, and Control*; Pearson: London, UK, 2001; ISBN 978-0-13-091014-1.
69. Bianco, E.; Rizzello, A.; Ferraris, A.; Carello, M. Modeling and experimental validation of vehicle's electric powertrain. In Proceedings of the 2022 IEEE International Conference on Environment and Electrical Engineering and 2022 IEEE Industrial and Commercial Power Systems Europe (EEEIC /I&CPS Europe), Prague, Czech Republic, 28 June–1 July 2022; pp. 1–6. [CrossRef]
70. Grano, E.; Bianco, E.; De Carvalho Pinheiro, H.; Carello, M. MTPA and flux weakening control of electric motors: A numerical approach. In Proceedings of the 2023 IEEE International Conference on Environment and Electrical Engineering and 2023 IEEE Industrial and Commercial Power Systems Europe (EEEIC/I&CPS Europe), Madrid, Spain, 6–9 June 2023; pp. 1–7. [CrossRef]

71. Muhlethaler, J.; Biela, J.; Kolar, J.W.; Ecklebe, A. Core Losses Under the DC Bias Condition Based on Steinmetz Parameters. *IEEE Trans. Power Electron.* **2012**, *27*, 953–963. [CrossRef]
72. Ciampolini, M.; Fazzini, L.; Berzi, L.; Ferrara, G.; Pugi, L. Simplified Approach for Developing Efficiency Maps of High-Speed PMSM Machines for Use in EAT Systems Starting from Single-Point Data. In Proceedings of the 2020 IEEE International Conference on Environment and Electrical Engineering and 2020 IEEE Industrial and Commercial Power Systems Europe (EEEIC/I&CPS Europe), Madrid, Spain, 9–12 June 2020; pp. 1–6. [CrossRef]
73. Stevens, J. Fundamentals of Thermal Resistance, HeatSink blog by Celsia. 2018. Available online: https://celsiainc.com/heat-sink-blog/fundamentals-of-thermal-resistance/ (accessed on 29 November 2023).
74. Wang, B.; Nie, Y.; Yang, Z.; Zong, C.; Geng, L. *Study on the Barycenter Position of Measurement and Data Processing for Dura-Axle Vehicle*; Atlantis Press: Amsterdam, The Netherlands, 2016; ISBN 978-94-6252-188-9. [CrossRef]
75. Zhao, X.; Kang, J.; Lei, T.; Wang, Y.; Cao, Z. Vehicle Centroid Measurement System Based On Forward Tilt Method Error Analysis. *IOP Conf. Ser. Mater. Sci. Eng.* **2018**, *452*, 042189. [CrossRef]
76. Pinheiro, H.d.C.; Messana, A.; Carello, M.; Rosso, N. Multibody Parameter Estimation: A Comprehensive Case-Study for an Innovative Rear Suspension. In Proceedings of the SAE BRASIL 2022 Congress, Sao Paulo, Brazil, 24–27 November 2022; SAE Technical Paper 2022-36-0059. SAE International: Sao Paulo, Brazil, 2023. [CrossRef]
77. Fehér, Á.; Aradi, S.; Bécsi, T. Hierarchical Evasive Path Planning Using Reinforcement Learning and Model Predictive Control. *IEEE Access* **2020**, *8*, 187470–187482. [CrossRef]
78. *BS ISO 3888-2:2011*; Passenger Cars—Test Track for a Severe Lane-Change Manoeuvre. ISO International Standards: Geneva, Switzerland, 2011.
79. De Carvalho Pinheiro, H.; Sisca, L.; Carello, M.; Ferraris, A.; Airale, A.G.; Falossi, M.; Carlevaris, A. *Methodology and Application on Load Monitoring Using Strain-Gauged Bolts in Brake Calipers*; SAE Technical Paper 2022-01-0922; SAE International: Warrendale, PA, USA, 2022. [CrossRef]